

Large valley Nernst effect in twisted multilayer graphene systems

Guanlin Jian(简冠林) Zhen-Gang Zhu(朱振刚), and Gang Su(苏刚)
Citation: Chin. Phys. B, 2023, 32 (**10**): 107202. DOI: 10.1088/1674-1056/acbd2c

Journal homepage: http://cpb.iphy.ac.cn; http://iopscience.iop.org/cpb

What follows is a list of articles you may be interested in

Emergence of correlations in twisted monolayer-trilayer graphene heterostructures

Zhang Zhou(周璋), Kenji Watanabe, Takashi Taniguchi, Xiao Lin(林晓), Jinhai Mao(毛金海), and Hong-Jun Gao(高鸿钧)
Chin. Phys. B, 2023, 32 (**9**): 097203. DOI: 10.1088/1674-1056/ace3a8

Controlled crossover of electron transport in graphene nanoconstriction: From Coulomb blockade to electron interference

Wei Yu(余炜), Xiao Guo(郭潇), Yuwen Cai(蔡煜文), Xiaotian Yu(俞晓天), and Wenjie Liang(梁文杰)
Chin. Phys. B, 2023, 32 (**7**): 077202. DOI: 10.1088/1674-1056/accf67

Tunable correlation in twisted monolayer-trilayer graphene

Dongdong Ding(丁冬冬), Ruirui Niu(牛锐锐), Xiangyan Han(韩香岩), Zhuangzhuang Qu(曲壮壮), Zhiyu Wang(王知雨), Zhuoxian Li(李卓贤), Qianling Liu(刘倩伶), Chunrui Han(韩春蕊), and Jianming Lu(路建明)
Chin. Phys. B, 2023, 32 (**6**): 067204. DOI: 10.1088/1674-1056/acc8c3

Long-range adsorbate interactions mediated by two-dimensional Dirac fermions

Xiaohui Wang(王晓慧), Zhen-Guo Fu(付振国), Zhigang Wang(王志刚), Feng Chi(迟锋), and Ping Zhang(张平)
Chin. Phys. B, 2023, 32 (**5**): 057201. DOI: 10.1088/1674-1056/acae77

Correlated states in alternating twisted bilayer-monolayer-monolayer graphene heterostructure

Ruirui Niu(牛锐锐), Xiangyan Han(韩香岩), Zhuangzhuang Qu(曲壮壮), Zhiyu Wang(王知雨), Zhuoxian Li(李卓贤), Qianling Liu(刘倩伶), Chunrui Han(韩春蕊), and Jianming Lu(路建明)
Chin. Phys. B, 2023, 32 (**1**): 017202. DOI: 10.1088/1674-1056/ac9de4

SPECIAL TOPIC — Valleytronics

Large valley Nernst effect in twisted multilayer graphene systems

Guanlin Jian(简冠林)[1], Zhen-Gang Zhu(朱振刚)[2,3,1,†], and Gang Su(苏刚)[4,1,3,‡]

[1] *School of Physical Sciences, University of Chinese Academy of Sciences, Beijing* 100049, *China*
[2] *School of Electronic, Electrical and Communication Engineering, University of Chinese Academy of Sciences, Beijing* 100049, *China*
[3] *CAS Center for Excellence in Topological Quantum Computation, University of Chinese Academy of Sciences, Beijing* 100190, *China*
[4] *Kavli Institute for Theoretical Sciences, University of Chinese Academy of Sciences, Beijing* 100190, *China*

(Received 15 October 2022; revised manuscript received 25 January 2023; accepted manuscript online 20 February 2023)

Valley Nernst effect is a newly proposed and experimentally confirmed effect, which could be used to design novel thermoelectric devices. We study the valley Nernst effect in $(M+N)$-layer twisted multilayer graphene systems by a simple low-energy effective model. It is found that the total valley Nernst coefficient (VNC) is three orders of magnitude larger than that in monolayer group-VI dichalcogenides. The total VNC increases with the increase of layer numbers. It is shown that the total VNC exhibits a structure with three peaks as a function of the Fermi energy. We identify that the central peak is always negative stemming from the flat band. Two shoulder peaks are positively induced by the conduction and valence bands, respectively. These predicted features can be tested experimentally. The present work would shed more light on valley caloritronics.

Keywords: valley Nernst effect, twisted multilayer graphene

PACS: 71.28.+d, 72.80.Vp **DOI:** 10.1088/1674-1056/acbd2c

1. Introduction

Thermoelectric power generation (TPG) is a powerful and ecological technique to generate electricity from waste or environmental heat by directly converting thermal energy to electric energy without any mechanical and chemical mediations. The conventional way of TPG is to utilize the Seebeck effect, which is a longitudinal effect describing an establishing electric field parallel to the applied temperature gradient. However, it is still a challenge to improve the dimensionless figure of merit ZT for getting a high energy conversion efficiency. On the other hand, a different pathway to realize high efficiency of the TPG via the anomalous Nernst effect has been emerging.[1,2] Compared to the Seebeck-effect-based TPG, the Nernst-effect-based TPG has a few advantages. Firstly, it can be applied to large size heat sources by making lateral thermopiles rather than the perpendicular thermopiles for the Seebeck-effect-based TPG. Secondly, the thermoelectric conversion for the Nernst-effect-based TPG can be related to the thermal conductivity (κ_{xx}) and electric conductivity (σ_{yy}) which are along or perpendicular to the temperature gradient (assume to be in x direction), respectively. It is well known that the Seebeck-effect-based TPG involves thermal conductivity (κ_{xx}) and electric conductivity (σ_{xx}) which are both along the direction of temperature gradient. However, the Wiedemann–Franz law tells us that $\kappa_{xx}/\sigma_{xx} = LT$, where L is the Lorentz number. Thus, the thermal conductivity and electric conductivity may not be tuned independently in the Seebeck-effect-based TPG. But they are not suffered the regulation from the Wiedemann–Franz law in the Nernst-effect-based TPG, because they are not in the same direction. This may provide us an extra freedom to tune the performance of the corresponding devices.[3] Therefore, this Nernst-effect-based TPG has great potential applications. The present challenge is that the Nernst coefficient is small in usual materials. For example, it is about 1 μV/K for FePt with a high uniaxial magnetic anisotropy.[4] This value is quite small so that it may not be used in realistic applications easily. Since the anomalous Nernst effect is closely determined by Berry curvature of Bloch bands in momentum space for its intrinsic mechanism, a higher Nernst coefficient may be achieved in materials with nontrivial topological properties. Recently, valley Nernst effect (VNE) has been proposed in monolayer group-VI dichalcogenides[5] and tested in experiment.[6] The VNE describes that charges from each valley make contribution to the anomalous Nernst coefficient due to nonvanishing Berry curvature in the valley. In the presence of time-reversal symmetry, different valleys possess opposite Berry curvatures leading to Nernst currents in the opposite directions. Therefore, the total Nernst coefficient from the two valleys is zero. If the valley degeneracy can be lifted, for example by straining the entire system, only one valley participates in the Nernst current, a nonzero total Nernst coefficient can be measured due to the single-valley-contribution which is a few orders of magnitude larger than that in NiFe in experiment.[6] Therefore, the VNE exhibits great potential

†Corresponding author. E-mail: zgzhu@ucas.ac.cn
‡Corresponding author. E-mail: gsu@ucas.ac.cn

© 2023 Chinese Physical Society and IOP Publishing Ltd

in TPG. This inspires us to seek for materials with even larger valley Nernst coefficient. We will show that the VNE is enhanced dramatically in twisted multilayer graphene (TMG).

Twisted bilayer graphene (TBG) has attracted much attention after the observation of the correlated insulating phases[7–11] and unconventional superconductivity.[9,12,13] The low-energy physics of twisted graphene systems are characterized by flat bands[14,15] around the "magic angles". The magic angle systems extend fast from TBG to twisted trilayer graphene,[16–21] twisted double bilayer graphene[22–27] and twisted multilayer graphene[28,29] in theoretical and experimental aspects. Experimentally, many strong correlated physics including Mott insulator, unconventional superconductivity, nematicity,[30–34] strange metal,[35,36] and ferromagnetism[8,37–41] were found in twisted bilayer graphene.[42–46] Theoretically, many low-energy effective models, such as tight-binding model,[28,47–51] effective Wannier tight-binding model,[52–59] density functional model,[60–62] and effective continuum model[14,15,63,64] were proposed to describe generic TBG systems. Based on these models, many theories have been proposed to calculate the property of twisted graphene systems and mainly to figure out the electronic structures,[16,55–58,65–70] the strong correlated phases[41,42,46,70–82] and the mechanism of unconventional superconductivity.[63,75,77,78,80,83–88]

In addition, topology, which is currently one of the key topics in condensed physics, also finds its importance in twisted electronics. Experimentally, the observation of hysteresis loops and chiral edge current of the TBG,[43] and more importantly, the observation of well-quantized resistance of the hBN-aligned TBG[39,43] demonstrates the existence of quantized anomalous Hall (QAH) state,[41,89] the topological phase, in twisted electronics. Theoretically, it was shown that the four low energy flat bands of twisted bilayer graphene have nontrivial topology,[69,90] more accurately the fragile topology,[24,58,69] because of their odd windings of Wilson loops.[65,78,91] The nontrivial topology of twisted bilayer graphene[92] is believed to originate from the equivalence between the four flat bands and the zeroth pseudo-Landau level with opposite Chern numbers and sublattice polarizations.[78,93] Also in TMG with N-layer graphene being placed with a twisted angle on M-layer graphene as shown in Fig. 1, two low energy flat bands for each valley exist. Moreover, Chern-number hierarchy in the $(M+N)$-layer TMG system was found.[29] The quantum valley Hall effect, orbital magnetism, and anomalous Hall effect[34,43] are believed to exist in the TMG. Furthermore, the valleytronics in two-dimensional materials based on manipulating the valley index is of great importance.[94–99] Motivated by these works, we study the anomalous valley Nernst effect of $(M+N)$-layer TMG systems. We find that the anomalous valley Nernst coefficient shows interesting and rich features with layer numbers, chirality, and temperature, especially for the flat bands.

2. Model and method

We study the $(M+N)$-layer TMG with the M-layer chirally stacked (the ABC stacking) graphene being placed on top of the other N-layer chirally stacked graphene. And the M-layer part is twisted by a nonvanishing angle θ with the other N-layer part, as schematically shown in Fig. 1(a) (for the case of $M=2$, $N=2$). The twisted angle obeys a relation $\cos\theta(m)=(3m^2+3m+1/2)/(3m^2+3m+1)$,[29] where m is a positive integer. In the TMG system, the unit cell for untwisted systems becomes now a moiré supercell for moiré superlattice so that the Brillouin zone (BZ) of the moiré supercell has been significantly reduced compared with those of the untwisted multilayers, as shown in Fig. 1(d). We study a model that describes the behavior of the system at the first magic angle of TBG $\theta=1.05^\circ$.[29] Specifically, from the perspective of the pseudo-Landau levels, in a multilayer system with chirality, almost flat pseudo-Landau levels of opposite Chern numbers will be generated. The two flat bands are pinned to zero energy and remain almost flat even after being coupled with other layers in the TMG systems as long as the chiral symmetry is preserved.[29,68] On this basis, we can construct the Hamiltonian by dividing the $(M+N)$-layer TMG system into three subsystems with the TBG as the interface of TMG, the $(M-1)$ layers below the TBG, and the $(N-1)$ layers above the TBG, as schematically shown in Fig. 1(c). Here we consider the K valley (Fig. 1(d)) only, and the effective Hamiltonian at K' valley can be obtained by applying a time reversal operation to that at the K valley.

We take a part of the system (three-layer graphene) shown in Fig. 1(e) as an example to explain the charality. The $+$ stacking chirality means that the B_1 sublattice of the upper layer is strongly coupled with the A_2 sublattice of the middle layer, forming pairs of bounding and antibounding states. And the B_2 sublattice of the middle layer is strongly coupled with the A_3 sublattice of the lower layer. For the schematic three-layer case in Fig. 1(e), the A_1 sublattice of the upper layer and the B_3 sublattice of the lower layer are left as two low-energy degrees of freedom. Similarly, the $-$ stacking chirality has the reversed A and B sublattice of the upper and lower layers as the two low-energy degrees of freedom. Thus, the low-energy effective Hamiltonian of the $(M-1)$-layer graphene around the K valley can be obtained by $(M-1)$-th order perturbation theory,[100] which gives

$$H^{\alpha}_{\text{eff}}(M-1)$$

$$= (-1)^{M-2} \begin{pmatrix} 0 & \dfrac{[\hbar v_{\rm F}(k_x + {\rm i}\alpha k_y)]^{M-1}}{t_\perp^{M-2}} \\ \dfrac{[\hbar v_{\rm F}(k_x - {\rm i}\alpha k_y)]^{M-1}}{t_\perp^{M-2}} & 0 \end{pmatrix}, \tag{1}$$

where $t_\perp$ is the interlayer hopping within the $(M-1)$-layer part and $\alpha = \pm$ is the stacking chirality associated with the M layers.

The low-energy effective degrees of freedom of the TBG at the interface around the K valley are two flat bands which are pinned to zero energy. So the corresponding low-energy effective Hamiltonian reads

$$H_{\rm TBG} = \begin{pmatrix} \varepsilon_1(k) & 0 \\ 0 & \varepsilon_2(k) \end{pmatrix}, \tag{2}$$

where $\varepsilon_1(k) = \varepsilon_2(k) = 0$.

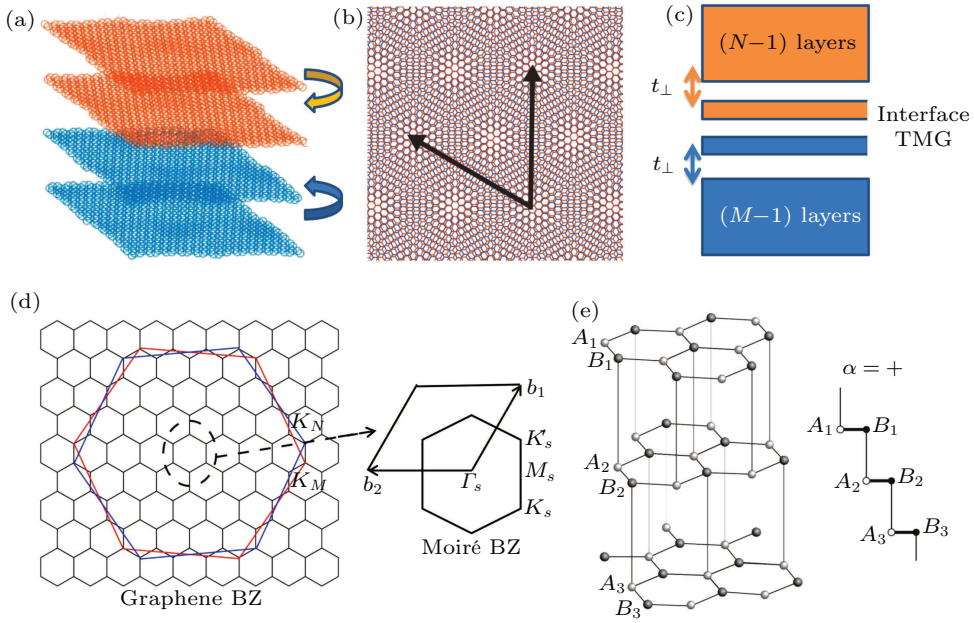


Fig. 1. (a) Structure of the twisted multilayer graphene with $M = 2$ and $N = 2$. (b) Moiré pattern of the twisted multilayer graphene, seen from the top. The two black arrows denote the lattice vectors of the moiré supercell. (c) A schematic illustration of the TMG system. (d) The Brillouin zones of the top N multilayers, bottom M multilayers, and the moiré supercell are plotted in red, blue, and black lines, respectively. K_N and K'_N are top N multiplayers graphene valleys. K_M and K'_M are bottom M multilayers graphene valleys.[29] (e) The ABC stacking with "+" chirality in graphene multilayers. The vertical lines are coupling between different layers. In "+" stacking chirality sublattices B_1A_2 and B_2A_3 are strongly coupled leaving A_1 and B_3 as two low-energy degrees of freedom. The "–" stacking chirality is obtained when reversing the sublattices A and B in the above sequence. This means for "–" stacking chirality sublattices A_1B_2, A_2B_3 are strongly coupled leaving B_1 and A_3 as two low-energy degrees of freedom.

Now we consider the coupling between the flat bands of the TBG and the $(M-1)$-layer part. If the stacking chirality is + as that in Fig. 1(e), the degree of freedom from the A sublattice (for example the A_1) of the upper-most atomic layer of the $(M-1)$-layer part is coupled to one of the two flat bands. After including this coupling between $(M-1)$-layer part and the flat bands from the interface TBG, the low-energy effective Hamiltonian around the moiré K_s point (contributed by the M-layer part) is now

$$H^{\alpha}_{K_s}(\boldsymbol{k}) = \begin{pmatrix} H^{\alpha}_{\rm eff}(M-1) & h_\alpha \\ h^{\dagger}_\alpha & H_{\rm TBG} \end{pmatrix}, \tag{3}$$

where h_α is the effective coupling with

$$h_+ = \begin{pmatrix} 0 & 0 \\ t_{\rm eff} & 0 \end{pmatrix} \tag{4}$$

and $h_- = h_+^{\dagger}$. Here $t_{\rm eff}$ is the low-energy effective coupling parameter between the states of the $(M-1)$-layer graphene and the flat bands from the interface TBG. Inserting Eqs. (1), (2), and (4) into Eq. (3), we obtain the low-energy effective Hamiltonian around the moiré K_s point

$$H^{\alpha}_{K_s}(\boldsymbol{k}) = \begin{pmatrix} 0 & \dfrac{(k_x + {\rm i}\alpha k_y)^{M-1}}{m_{M-1}} & 0 \\ \dfrac{(k_x + {\rm i}\alpha k_y)^{M-1}}{m_{M-1}} & 0 & t_{\rm eff} \\ 0 & t_{\rm eff} & 0 \end{pmatrix}, \tag{5}$$

where

$$m_{M-1} = \frac{t_\perp^{M-1}}{(-1)^{M-2}(\hbar v_{\rm F})^{M-1}}. \tag{6}$$

Similarly, the low-energy effective Hamiltonian around the moiré K'_s point is

$$H^{\alpha'}_{K'_s}(\boldsymbol{k}) = \begin{pmatrix} 0 & \dfrac{(k_x + {\rm i}\alpha' k_y)^{N-1}}{m_{N-1}} & t_{\rm eff} \\ \dfrac{(k_x + {\rm i}\alpha' k_y)^{N-1}}{m_{N-1}} & 0 & 0 \\ t_{\rm eff} & 0 & 0 \end{pmatrix}, \tag{7}$$

where $\alpha' = \pm$ is the stacking chirality of the N layers and m_{N-1} is given by Eq. (6). Here we should point out that the

twisted angle θ doesn't enter into the Hamiltonian directly. It gives rise to redefinition of the momentum in the first BZ from the moiré supercell. The moiré effects in these equations are embodied in the two flat bands. The interlayer coupling parameter $t_{\rm eff}$ basically contains the effect of the twisted angle. However we treat it as a fitting parameter and the entire study is valid at the first magic angle, i.e., $\theta = 1.05^\circ$. We can solve Eqs. (5) and (7) analytically. The eigenenergies of Eq. (5) are expressed as

$$\begin{aligned}
&\varepsilon_{1\boldsymbol{k}}(M-1) = -\sqrt{\frac{k^{2M-2}}{m_{M-1}^2} + |\, t_{\rm eff}\,|^2},\\
&\varepsilon_{2\boldsymbol{k}} = 0,\\
&\varepsilon_{3\boldsymbol{k}}(M-1) = \sqrt{\frac{k^{2M-2}}{m_{M-1}^2} + |\, t_{\rm eff}\,|^2}.
\end{aligned} \tag{8}$$

The eigenenergies of Eq. (7) have the same expression but with $(M-1)$ replaced by $(N-1)$. The eigenstates of $H^{\alpha}_{K_s}(\boldsymbol{k})$ are expressed as

$$\begin{aligned}
|\,\Psi^{M-1}_{1\boldsymbol{k}}\rangle &= \left(\frac{(k_x+{\rm i}\alpha k_y)^{M-1}}{\sqrt{2}g_{M-1}(|\,\boldsymbol{k}\,|)}, -\frac{1}{\sqrt{2}}, \frac{\tilde{t}_{\rm eff}}{\sqrt{2}g_{M-1}(|\,\boldsymbol{k}\,|)}\right)^{\rm T},\\
|\,\Psi^{M-1}_{2\boldsymbol{k}}\rangle &= \left(\frac{\tilde{t}_{\rm eff}\,{\rm e}^{{\rm i}\alpha\theta_k(M-1)}}{g_{M-1}(|\,\boldsymbol{k}\,|)}, 0, \frac{|\,\boldsymbol{k}\,|^{M-1}}{g_{M-1}(|\,\boldsymbol{k}\,|)}\right)^{\rm T},\\
|\,\Psi^{M-1}_{3\boldsymbol{k}}\rangle &= \left(\frac{(k_x+{\rm i}\alpha k_y)^{M-1}}{\sqrt{2}g_{M-1}(|\,\boldsymbol{k}\,|)}, \frac{1}{\sqrt{2}}, \frac{\tilde{t}_{\rm eff}}{\sqrt{2}g_{M-1}(|\,\boldsymbol{k}\,|)}\right)^{\rm T},
\end{aligned} \tag{9}$$

where $g_{M-1}(|\boldsymbol{k}|) = \sqrt{\tilde{t}^2_{\rm eff} + |\boldsymbol{k}|^{2M-2}}$, $\tilde{t}_{\rm eff} = t_{\rm eff}/m_{M-1}$, and $\theta_k = \arctan(k_y/k_x)$. The eigenstates of $H^{\alpha'}_{K'_s}(\boldsymbol{k})$ are expressed as

$$\begin{aligned}
|\,\Psi^{N-1}_{1\boldsymbol{k}}\rangle &= \left(-\frac{1}{\sqrt{2}}, \frac{(k_x-{\rm i}\alpha' k_y)^{N-1}}{\sqrt{2}g_{N-1}(|\,\boldsymbol{k}\,|)}, \frac{\tilde{t}_{\rm eff}}{\sqrt{2}g_{N-1}(|\,\boldsymbol{k}\,|)}\right)^{\rm T},\\
|\,\Psi^{N-1}_{2\boldsymbol{k}}\rangle &= \left(0, -\frac{\tilde{t}_{\rm eff}\,{\rm e}^{-{\rm i}\alpha'\theta_k(N-1)}}{g_{N-1}(|\,\boldsymbol{k}\,|)}, \frac{|\,\boldsymbol{k}\,|^{N-1}}{g_{N-1}(|\,\boldsymbol{k}\,|)}\right)^{\rm T},\\
|\,\Psi^{N-1}_{3\boldsymbol{k}}\rangle &= \left(\frac{1}{\sqrt{2}}, \frac{(k_x-{\rm i}\alpha' k_y)^{N-1}}{\sqrt{2}g_{N-1}(|\,\boldsymbol{k}\,|)}, \frac{\tilde{t}_{\rm eff}}{\sqrt{2}g_{N-1}(|\,\boldsymbol{k}\,|)}\right)^{\rm T}.
\end{aligned} \tag{10}$$

The Berry curvature[101] is determined by $\Omega_{nk}(M) = \hat{z}\cdot\nabla_{\boldsymbol{k}} \times \langle\Psi^{M-1}_{n\boldsymbol{k}}|{\rm i}\nabla_{\boldsymbol{k}}|\Psi^{M-1}_{n\boldsymbol{k}}\rangle$ for 2D materials,where $\nabla_{\boldsymbol{k}}$ means directional derivatives with respect to the momentum $\boldsymbol{k}$, and $\Psi^{M-1}_{n\boldsymbol{k}}$ is the periodic part of the Bloch function. For the low-energy effective Hamiltonian around the moiré K_s point described by Eq. (5), the Berry curvatures of conduction band (subscript index 1), flat band (subscript index 2) and valence band (subscript index 3) are respectively given by

$$\begin{aligned}
\Omega_{1M}(\boldsymbol{k}) &= \Omega_{3M}(\boldsymbol{k}) = \frac{-\alpha(M-1)^2k^{2M-4}}{(t_{\rm eff}m_{M-1})^2 + k^{2M-2}}\\
&\quad + \frac{\alpha(M-1)^2k^{4M-6}}{[(t_{\rm eff}m_{M-1})^2 + k^{2M-2}]^2},\\
\Omega_{2M}(\boldsymbol{k}) &= \frac{2\alpha(t_{\rm eff}m_{M-1})^2(M-1)^2k^{2M-4}}{[(t_{\rm eff}m_{M-1})^2 + k^{2M-2}]^2}.
\end{aligned} \tag{11}$$

Similarly, for the low-energy effective Hamiltonian around the moiré K'_s point described by Eq. (7), the Berry curvatures of conduction band (subscript index 1), flat band (subscript index 2) and valence band (subscript index 3) are derived as

$$\begin{aligned}
\Omega_{1N}(\boldsymbol{k}) &= \Omega_{3N}(\boldsymbol{k}) = \frac{\alpha'(N-1)^2k^{2N-4}}{(t_{\rm eff}m_{N-1})^2 + k^{2N-2}}\\
&\quad + \frac{-\alpha'(N-1)^2k^{4N-6}}{[(t_{\rm eff}m_{N-1})^2 + k^{2N-2}]^2},\\
\Omega_{2N}(\boldsymbol{k}) &= \frac{-2\alpha'(t_{\rm eff}m_{N-1})^2(N-1)^2k^{2N-4}}{[(t_{\rm eff}m_{N-1})^2 + k^{2N-2}]^2}.
\end{aligned} \tag{12}$$

When a temperature gradient is applied, an electric field develops in the opposite direction because of the Seebeck effect. Besides the parallel effect, in the presence of the temperature gradient, the electrons experience a Lorentz-like force and thus move in the direction perpendicular to the diffusion current, which is the anomalous Nernst coefficient effect (ANE) induced by the intrinsic nonvanishing Berry curvature. This is also the intrinsic mechanism contributing to the anomalous Hall resistivity.[101,102] Thus, the velocity multiplied by the entropy density gives rise to the anomalous Nernst coefficient (ANC)[5] around moiré K_s and moiré K'_s points

$$\beta_n^{M(N)} = 4\pi\beta_0 \int \frac{{\rm d}^2\boldsymbol{k}}{(2\pi)^2}\Omega_{nM(N)}(\boldsymbol{k})S_{nM(N)}(\boldsymbol{k}), \tag{13}$$

where $n = 1,2,3$ represent the conduction band, flat band, and valence band, respectively. $\beta_0 = (ek_{\rm B}/2h)$, e is the electron charge, h is the Planck constant, $S_{nM}(\boldsymbol{k}) = -f_{nM\boldsymbol{k}}\ln f_{nM\boldsymbol{k}} - (1-f_{nM\boldsymbol{k}})\ln(1-f_{nM\boldsymbol{k}})$ (Boltzmann constant $k_{\rm B}$ has been absorbed in β_0) is the entropy density for moiré K_s point and n-band, and $f_{nM\boldsymbol{k}}$ is the Fermi distribution function. The entropy density develops a peak when the eigenenergies match the chemical potentials μ, and is essentially zero when the energy is beyond the range of $[\mu - 5k_{\rm B}T, \mu + 5k_{\rm B}T]$. The integration is performed over the neighborhood of moiré K_s (K'_s) point in the momentum space. $\Omega_{nM}(\boldsymbol{k})$ and $S_{nM}(\boldsymbol{k})$ can be expressed as functions of the modulus of the wave vector $\boldsymbol{k}$. For the flat bands, we make the integration in the entire moiré Brillioun zone:

$$\beta_2^{M(N)} = 4\pi\beta_0 \int \frac{{\rm d}^2\boldsymbol{k}}{(2\pi)^2}\Omega_{2M(N)}(\boldsymbol{k})S_{2M(N)}(\boldsymbol{k}), \tag{14}$$

where $\boldsymbol{k}$ takes values in the entire moiré Brillioun zone. For the conduction and valence bands, we can use the Debye model,[103,104] namely, the integration is taken in a circular region centered at moiré K_s (K'_s) point and the area is equal to the half of the first moiré Brillouin zone for moiré K_s (K'_s) point. Thus, Eq. (13) can be written as

$$\beta_n^{M(N)} = 2\beta_0 \int_0^{k_{\rm c}} \Omega_{nM(N)}(k)S_{nM(N)}(k)k\,{\rm d}k, \tag{15}$$

where $k_c = \frac{2\sqrt{\pi}}{3^{3/4}a/[2\sin(\theta/2)]}$, and $n = 1,3$. Here we call β_n^M (β_n^N) the one band VNC. The valley Nernst coefficient (VNC) around moiré point K_s and point K_s' are, respectively,

$$\beta^{M(N)} = \beta_1^{M(N)} + \beta_2^{M(N)} + \beta_3^{M(N)}. \tag{16}$$

For brevity, we call β^M (β^N) the one moiré point VNC.

The total VNC is composed of the contributions of all crystals, i.e., $\beta_T = \beta^M + \beta^N$, we have

$$\begin{aligned}\beta_T = {} & 4\pi\beta_0 \int \frac{d^2\boldsymbol{k}}{(2\pi)^2} [\Omega_{2M}(\boldsymbol{k})S_{2M}(\boldsymbol{k}) + \Omega_{2N}(\boldsymbol{k})S_{2N}(\boldsymbol{k})] \\ & + 2\beta_0 \int_0^{k_c} k\,dk[\Omega_{1M}(k)S_{1M}(k) + \Omega_{1N}(k)S_{1N}(k) \\ & + \Omega_{3M}(k)S_{3M}(k) + \Omega_{3N}(k)S_{3N}(k)]. \end{aligned} \tag{17}$$

The total flat band VNC is given by $\beta_F = \beta_2^M + \beta_2^N$, so we have

$$\beta_F = 4\pi\beta_0 \int \frac{d^2\boldsymbol{k}}{(2\pi)^2} [\Omega_{2M}(\boldsymbol{k})S_{2M}(\boldsymbol{k}) + \Omega_{2N}(\boldsymbol{k})S_{2N}(\boldsymbol{k})]. \tag{18}$$

The VNC from the conduction and valence bands is then

$$\beta_{CV} = \beta_T - \beta_F. \tag{19}$$

For brevity, we call β_{CV} as the conduction-valence band VNC.

3. Results and analysis

The magnitude of the VNE is determined by the VNC. In the following, we investigate the properties of the VNC for the valley K for a freestanding layer. Corresponding to the valley K, there is a full first moiré Brillouin zone with moiré K_s and moiré K_s' points around where the energy bands are corresponding to up N layers and down M layers in our chosen model. For each moiré K_s (K_s') point there are three bands, the conduction band, flat band and valence band. All six bands VNC should be considered since the valence band, the conduction band, and the flat bands are close to the Fermi level, and may all contribute to the VNC. Specifically, we calculate the total VNC β_T, β_F and the conduction-valence band VNC β_{CV} to clearly reveal their contributions respectively. In our calculation, parameters are taken as follows: the interlayer hopping in the $(M-1)$ layers $t_\perp = 0.001$ eV, the low-energy effective coupling between the states of the $(M-1)$ layers and the flat bands $t_{eff} = 0.01$ eV, the Fermi velocity $v_F = 10^{16}$ Å/s, graphene lattice constant $a = 2.46$ Å, the Boltzmann constant $k_B = 0.8629 \times 10^{-4}$ eV/K, and the Plank constant $\hbar = 0.6582 \times 10^{-15}$ eV·s.

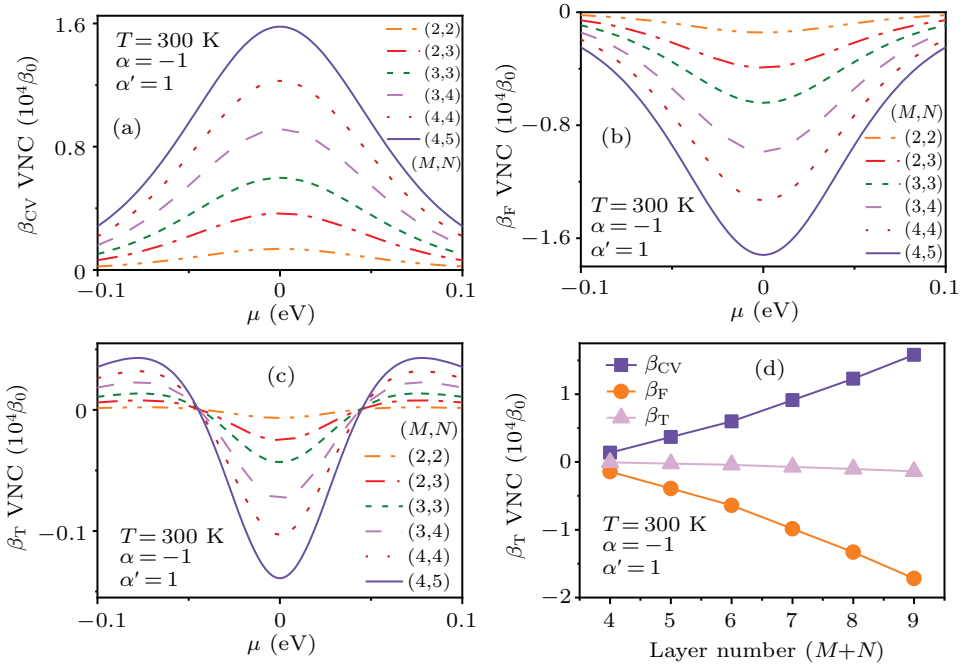


Fig. 2. The valley anomalous Nernst coefficient as a function of the Fermi energy for different layers at 150 K with M-layer chirality $\alpha = 1$ and the N-layer chirality $\alpha' = -1$. Here (M,N) means the layer number of (2,2), (2,3), (3,3), (3,4), (4,4), (4,5) corresponding to $M = 2$, $N = 2$; $M = 2$, $N = 3$; $M = 3$, $N = 3$; $M = 3$, $N = 4$; $M = 4$, $N = 4$; $M = 4$, $N = 5$, respectively. (a) The total flat band VNC β_F. (b) The conduction-valence band VNC β_{CV}. (c) The total VNC β_T. (d) The maximum values of the total VNC β_T, the total flat band VNC β_F and the conduction-valence band VNC β_{CV} as a function of layer number $(M+N)$.

In Fig. 2, we show how β_T, β_F and β_{CV} vary with TMG layers at the temperature of 300 K. The layer number $(M+N)$ changes from 4 to 9, corresponding to $M = 2$, $N = 2$; $M = 2$, $N = 3$; $M = 3$, $N = 3$; $M = 3$, $N = 4$; $M = 4$, $N = 4$; and $M = 4$, $N = 5$. We take the M-layer chirality $\alpha = 1$ and the N-layer chirality $\alpha' = -1$ in all these conditions. In the following discussion, the chirality condition will keep the same. If the sign of chirality is changed, the sign of VNC will be changed but the value keeps the same. In Fig. 2(c), we find that the value of the total VNC (β_T) for TMG at least can reach $-66.19\beta_0$

(the peak value of $2+2$ TMG) that is three orders of magnitude larger than that of MoS_2 which is $0.14\beta_0$[5,104] at room temperature. The large value of β_T for TMG is expected because two low-energy bands in the TMG system possess valley Chern numbers that are dependent on both the number of layers and the stacking chiralities.[29] From Fig. 2, it is observed that the absolute value of the total VNC β_T, the total flat VNC β_F and the conduction-valence VNC β_{CV} all increase with the increase of the layer number. β_{CV} is positive; while β_F takes negative values. The total flat VNC β_F and the conduction-valence VNC β_{CV} increase much faster than that of the total VNC β_T. The increase of VNC by stacking more layers can be understood simply as the Berry curvature is also increased. Although the stacked more layers are not adjacent to the interface TBG, they are effectively coupled to the interface TBG via the layers in-between these stacked more layers and the interface TBG. However, this intuitively simple scenario may not be extended to an infinite-layer system since the VNC cannot be increased to infinity. This indicates that there is a limitation on the studied model that may not be applicable to the cases of very large M and N. For the very large $M+N$ case, the situation becomes very complicated and is beyond our study. This can be left for further explorations. The observations of VNC shown in Fig. 2 are consistent with the valley Chern numbers of TMG derived in Ref. [29] in which the valley Chern numbers increase with the increase of the layer number. This means one can enhance the valley Nernst effect by simply increasing the thickness of the TMG.

The $(M+N)$-layer TMG systems are divided into the M-layer part and the N-layer part, so we have different layer-number combinations corresponding to different systems for a fixed total layer number. For example, total 5-layer TMG systems have two different situations: $M=3$, $N=2$ and $M=2$, $N=3$. In Fig. 3, we show the variation of the total VNC β_T with respect to μ. Two features can be summarized in the following. Firstly, if we only exchange the layer number M and the layer number N, the total VNC keeps the same. For example, the total VNC of the system with $M=3$, $N=2$ ($M=4$, $N=3$) is exactly the same as that of the system with $M=2$, $N=3$ ($M=3$, $N=4$). Secondly, for the same total number of layers, when the difference between M and N is larger, the total VNC absolute value becomes slightly larger. For example, as seen in Fig. 3(d), the total VNC of the system with $M=3$, $N=5$ (or $M=5$, $N=3$) is a little larger than that of the system with $M=4$, $N=4$; while the total VNC of the system with $M=2$, $N=6$ (or $M=6$, $N=2$) is larger than that of the system with $M=3$, $N=5$ (or $M=5$, $N=3$). But generally, Fig. 3 shows that different lines nearly overlap with each other, which means with the fixed total layer number, the total VNC of the system with different M-layer part and N-layer part are nearly the same. The results are roughly consistent with Ref. [29] in which the valley Chern numbers are fixed by the total layer number.

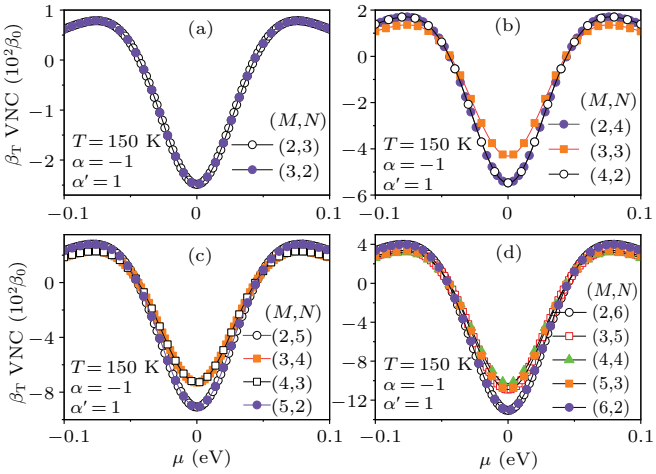


Fig. 3. The anomalous Nernst coefficient as a function of the Fermi energy with the same total layer number $(M+N)$ but different M-layer number and N-layer number. The total ANC β_T is calculated at temperature of 150 K with M-layer chirality $\alpha=1$ and the N-layer chirality $\alpha'=-1$. The total layer numbers $(M+N)$ for (a), (b), (c) and (d) are 5, 6, 7 and 8, respectively.

Now let us investigate the properties of VNC relating to the temperature. To be more specific, we calculate the one-flat band VNC β_2^M (see Eq. (13)) and the one-conduction band VNC β_1^M around moiré K_s of the TMG system with $M=2$. Figure 4(a) displays the broadening of the peak of β_2^M around zero Fermi energy at higher temperature. It is interesting to note that the maximum value of β_2^M does not change with temperature. In Fig. 4(b), the one-conduction band VNC β_1^M has a similar broadening of the peak, but its maximum value increases with increasing temperature. This different property of maximum values between flat band and the one-conduction band results from the fact that the Fermi distribution function $f_{nM\boldsymbol{k}}=0.5$ is independent of temperature for flat band because when $\mu=\varepsilon_{2\boldsymbol{k}}=0$ we have $(\mu-\varepsilon_{2\boldsymbol{k}})/T=0$.

We have discussed the behavior of the VNC at relatively high temperature. We should emphasize that the relatively high temperature induces a mixing contribution of different bands to the VNC. It is possible to distinguish their single role in the VNC at relatively low temperature. Figure 5 shows the low temperature VNC β^M in Eq. (16) around one moiré point K_s. The β^M is composed of three contributions: conduction band, flat band and valence band. The main feature is the three-peak structure where a main peak is around at the center (around $\mu=0$) with negative value, and two shoulder peaks with positive values locate at a higher and a lower Fermi energy. We should point out that the central peak is induced by the flat band, and the right (left) peak stems from the conduction (valence) band. Because the flat band VNC and the conduction (valence) band VNC have opposite signs, the magnitude of the central peak (the total VNC) is slightly decreased with increasing temperature. Thus at sufficiently low

temperature, the central peak and shoulder peaks are separated completely because of the gap between the flat band and conduction (valence) band.

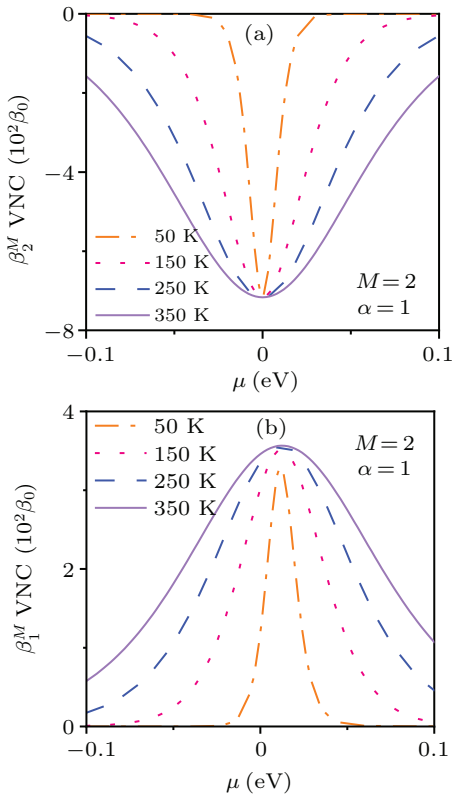


Fig. 4. The anomalous Nernst coefficient as a function of the Fermi energy with different temperatures. Here the total layer number is 4 with $2M$ layers and the M-layer chirality $\alpha = 1$. (a) The one flat band ANC β_2^M in Eq. (13). (b) The one conduction band ANC β_1^M in Eq. (13).

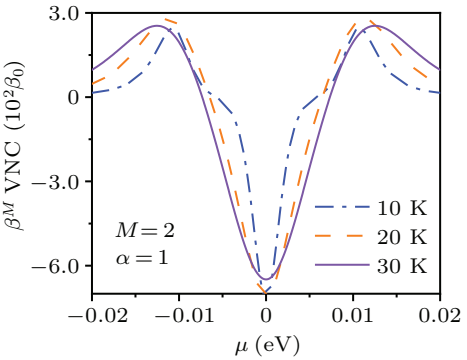


Fig. 5. The VNC β^M in Eq. (16) around moiré point K_s as a function of the Fermi energy with different low temperatures.

In the following, we want to estimate the critical temperature below which the three-peak structure can almost fully be distinct. In Fig. 5, the temperature is 30 K, and the three-peak structure can only be distinguished approximately. It is known that the entropy density is essentially zero when the energy is beyond the range of $[\mu - 5k_BT, \mu + 5k_BT]$.[5] So when the range of $10k_BT$ is smaller than the energy gap (in our model the energy gap equals to t_{eff}), the contribution from different bands to the one moiré point VNC can be clearly separated. Therefore, by $10k_BT = t_{\text{eff}} = 0.01$ eV, we estimate this critical temperature to be 11.63 K below which the three peaks can be fully separated and the predicted feature in this work can be more easily tested.

4. Summary and discussion

In this paper, we have studied the valley Nernst coefficient (VNC) of $(M+N)$-layer TMG systems and found that the total VNC is three orders of magnitude larger than that in monolayer group-VI dichalcogenides. We should emphasize that there are many ways of multilayer graphene stacking leading to different systems, for example, trilayers in which one of the three layers is twisted by a small angle relative to perfect AAA, ABA, or ABC stacking,[105] the three-layer configurations corresponding to a twisted monolayer on a bilayer of graphene, the four-layer configurations including a twisted monolayer on a trilayer, and a twisted bilayer on a bilayer and so on.[106] Different stacking leads to different systems with different properties. Our study is only applicable to gaped systems, specifically for the system we described. To know clearly the behavior of the VNC, we take into account the contributions from moiré points K_s and K_s', and three energy bands (i.e., the conduction, flat and valence bands). We find that the total VNC is quite huge, which is at least three orders of magnitude larger than that for two-dimensional MoS_2-like materials. The reason might be that the energy gap of TMG is much smaller than that of MoS_2-like materials which gives rise to much larger Berry curvature for TMG. It is found that the total, flat-band, and conduction-valence band VNC all increase with increasing layer number. Here we have to point out that when layer number $(M+N)$ is large enough then we can not regard the present TMG as a two-dimensional system. When stacking more layers, the coupling between these extra layers and the twisted layers is reasonably assumed to be smaller and smaller. In this case, the twisted effect on the VNC may be decreasing. Thus, our conclusions may only be applicable to the systems with finite layers.

At sufficiently low temperature, the contributions from the conduction, flat and valence bands can be clearly separated, manifesting a larger total VNC because of lacking offset. These results are expected to be tested in near future experiments. This work presents a huge valley Nernst effect in TMG systems, which would have potential applications in designing novel thermoelectric devices.

Acknowledgements

Project supported in part by the National Key R&D Program of China (Grant No. 2018YFA0305800) and the National Natural Science Foundation of China (Grant Nos. 11974348 and 11834014). It is also supported by the Strategic Priority Research Program of Chinese Academy of Sciences (Grant

Nos. XDB28000000 and XDB33000000). ZGZ is supported in part by the Training Program of Major Research plan of the National Natural Science Foundation of China (Grant No. 92165105) and CAS Project for Young Scientists in Basic Research (Grant No. YSBR-057).

References

[1] Sakuraba Y, Hasegawa K, Mizuguchi M, Kubota T, Mizukami S, Miyazaki T and Takanashi K 2013 *Appl. Phys. Express* **6** 033003
[2] Sakuraba Y 2016 *Scripta Materialia* **111** 29
[3] Mizuguchi M and Nakatsuji S 2018 *Sci. Tech. Adv. Mater.* **20** 262
[4] Mizuguchi M, Ohata S, Uchida K I, Saitoh E and Takanashi K 2012 *Appl. Phys. Express* **5** 093002
[5] Yu X Q, Zhu Z G, Su G and Jauho A P 2015 *Phys. Rev. Lett.* **115** 246601
[6] Dau M T, Vergnaud C, Marty A, Beigne C, Gambarelli S, Maurel V, Journot T, Hyot B, Guillet T, Grevin B, *et al*. 2019 *Nat. Commun.* **10** 5796
[7] Cao Y, Fatemi V, Demir A, Fang S, Tomarken S L, Luo J Y, Sanchez-Yamagishi J D, Watanabe K, Taniguchi T, Kaxiras E, Ashoori R C and Jarillo-Herrero P 2018 *Nature* **556** 80
[8] Sharpe A L, Fox E J, Barnard A W, Finney J, Watanabe K, Taniguchi T, Kastner M A and Goldhaber-Gordon D 2019 *Science* **365** 605
[9] Codecido E, Wang Q, Koester R, Che S, Tian H, Lv R, Tran S, Watanabe K, Taniguchi T, Zhang F, Bockrath M and Lau C N 2019 *Sci. Adv.* **5** eaaw9770
[10] Choi Y, Kemmer J, Peng Y, Thomson A, Arora H, Polski R, Zhang Y, Ren H, Alicea J, Refael G, von Oppen F, Watanabe K, Taniguchi T and Nadj-Perge S 2019 *Nat. Phys.* **15** 1174
[11] Kerelsky A, McGilly L J, Kennes D M, Xian L, Yankowitz M, Chen S, Watanabe K, Taniguchi T, Hone J, Dean C, Rubio A and Pasupathy A N 2019 *Nature* **572** 95
[12] Cao Y, Fatemi V, Fang S, Watanabe K, Taniguchi T, Kaxiras E and Jarillo-Herrero P 2018 *Nature* **556** 43
[13] Yankowitz M, Chen S, Polshyn H, Zhang Y, Watanabe K, Taniguchi T, Graf D, Young A F and Dean C R 2019 *Science* **363** 1059
[14] dos Santos J M B L, Peres N M R and Neto A H C 2007 *Phys. Rev. Lett.* **99** 256802
[15] Bistritzer R and MacDonald A H 2011 *Proc. Natil. Acad. Sci. USA* **108** 12233
[16] Po H C, Zou L, Vishwanath A and Senthil T 2018 *Phys. Rev. X* **8** 031089
[17] Chen G, Jiang L, Wu S, Lyu B, Li H, Chittari B L, Watanabe K, Taniguchi T, Shi Z, Jung J, Zhang Y and Wang F 2019 *Nat. Phys.* **15** 237
[18] Chen G, Sharpe A L, Gallagher P, Rosen I T, Fox E J, Jiang L, Lyu B, Li H, Watanabe K, Taniguchi T, Jung J, Shi Z, Goldhaber-Gordon D, Zhang Y and Wang F 2019 *Nature* **572** 215
[19] Chen G, Sharpe A L, Fox E J, Zhang Y H, Wang S, Jiang L, Lyu B, Li H, Watanabe K, Taniguchi T, Shi Z, Senthil T, Goldhaber-Gordon D, Zhang Y and Wang F 2020 *Nature* **579** 56
[20] Zuo W J, Qiao J B, Ma D L, Yin L J, Sun G, Zhang J Y, Guan L Y and He L 2018 *Phys. Rev. B* **97** 035440
[21] Zhu Z, Carr S, Massatt D, Luskin M and Kaxiras E 2020 *Phys. Rev. Lett.* **125** 116404
[22] Chebrolu N R, Chittari B L and Jung J 2019 *Phys. Rev. B* **99** 235417
[23] Lee J Y, Khalaf E, Liu S, Liu X, Hao Z, Kim P and Vishwanath A 2019 *Nat. Commun.* **10** 5333
[24] Zhang Y H, Mao D, Cao Y, Jarillo-Herrero P and Senthil T 2019 *Phys. Rev. B* **99** 075127
[25] Cao Y, Rodan-Legrain D, Rubies-Bigorda O, Park J M, Watanabe K, Taniguchi T and Jarillo-Herrero P 2020 *Nature* **583** 215
[26] Shen C, Chu Y, Wu Q, Li N, Wang S, Zhao Y, Tang J, Liu J, Tian J, Watanabe K, Taniguchi T, Yang R, Meng Z Y, Shi D, Yazyev O V and Zhang G 2020 *Nat. Phys.* **16** 520
[27] Liu X, Hao Z, Khalaf E, Lee J Y, Ronen Y, Yoo H, Najafabadi D H, Watanabe K, Taniguchi T, Vishwanath A and Kim P 2020 *Nature* **583** 221
[28] Vela A, Moutinho M V O, Culchac F J, Venezuela P and Capaz R B 2018 *Phys. Rev. B* **98** 155135
[29] Liu J, Ma Z, Gao J and Dai X 2019 *Phys. Rev. X* **9** 031021
[30] Liu X, Wang Z, Watanabe K, Taniguchi T, Vafek O and Li J 2021 *Science* **371** 1261
[31] Jin C, Tao Z, Li T, Xu Y, Tang Y, Zhu J, Liu S, Watanabe K, Taniguchi T, Hone J C, Fu L, Shan J and Mak K F 2021 *Nat. Mater.* **20** 940
[32] Chichinadze D V, Classen L and Chubukov A V 2020 *Phys. Rev. B* **101** 224513
[33] Dodaro J F, Kivelson S A, Schattner Y, Sun X Q and Wang C 2018 *Phys. Rev. B* **98** 075154
[34] Chichinadze D V, Classen L and Chubukov A V 2020 *Phys. Rev. B* **102** 125120
[35] Cha P, Patel A A and Kim E A 2021 *Phys. Rev. Lett.* **127** 266601
[36] Cao Y, Chowdhury D, Rodan-Legrain D, Rubies-Bigorda O, Watanabe K, Taniguchi T, Senthil T and Jarillo-Herrero P 2020 *Phys. Rev. Lett.* **124** 076801
[37] Saito Y, Ge J, Rademaker L, Watanabe K, Taniguchi T, Abanin D A and Young A F 2021 *Nat. Phys.* **17** 478
[38] Repellin C, Dong Z, Zhang Y H and Senthil T 2020 *Phys. Rev. Lett.* **124** 187601
[39] Wu F and Sarma S D 2020 *Phys. Rev. Lett.* **124** 046403
[40] Saito Y, Ge J, Rademaker L, Watanabe K, Taniguchi T, Abanin D A and Young A F 2021 *Nat. Phys.* **17** 478
[41] Bultinck N, Chatterjee S and Zaletel M P 2020 *Phys. Rev. Lett.* **124** 166601
[42] Zhang Z, Myers R, Watanabe K, Taniguchi T and LeRoy B J 2020 *Phys. Rev. Research* **2** 033181
[43] Serlin M, Tschirhart C L, Polshyn H, Zhang Y, Zhu J, Watanabe K, Taniguchi T, Balents L and Young A F 2019 *Science* **367** 900
[44] Arora H S, Polski R, Zhang Y, Thomson A, Choi Y, Kim H, Lin Z, Wilson I Z, Xu X, Chu J H, Watanabe K, Taniguchi T, Alicea J and Nadj-Perge S 2020 *Nature* **583** 379
[45] Stepanov P, Das I, Lu X, Fahimniya A, Watanabe K, Taniguchi T, Koppens F H L, Lischner J, Levitov L and Efetov D K 2020 *Nature* **583** 375
[46] Liu X, Wang Z, Watanabe K, Taniguchi T, Vafek O and Li J I A 2021 *Science* **371** 1261
[47] Li Y and Koshino M 2019 *Phys. Rev. B* **99** 075438
[48] Wang Z F, Liu F and Chou M Y 2012 *Nano Lett.* **12** 3833
[49] Morell E S, Correa J D, Vargas P, Pacheco M and Barticevic Z 2010 *Phys. Rev. B* **82** 121407
[50] Shallcross S, Sharma S, Kandelaki E and Pankratov O A 2010 *Phys. Rev. B* **81** 165105
[51] Lin X and Tománek D 2018 *Phys. Rev. B* **98** 081410
[52] Hejazi K, Chen X and Balents L 2021 *Phys. Rev. Res.* **3** 013242
[53] Vafek O and Kang J 2021 *Phys. Rev. B* **104** 075143
[54] Zou L, Po H C, Vishwanath A and Senthil T 2018 *Phys. Rev. B* **98** 085435
[55] Yuan N F Q and Fu L 2018 *Phys. Rev. B* **98** 045103
[56] Koshino M, Yuan N F, Koretsune T, Ochi M, Kuroki K and Fu L 2018 *Phys. Rev. X* **8** 031087
[57] Kang J and Vafek O 2018 *Phys. Rev. X* **8** 031088
[58] Po H C, Zou L, Senthil T and Vishwanath A 2019 *Phys. Rev. B* **99** 195455
[59] Carr S, Fang S, Po H C, Vishwanath A and Kaxiras E 2019 *Phys. Rev. Res.* **1** 033072
[60] Uchida K, Furuya S, Iwata J I and Oshiyama A 2014 *Phys. Rev. B* **90** 155451
[61] Kang P, Zhang W T, Michaud-Rioux V, Kong X H, Hu C, Yu G H and Guo H 2017 *Phys. Rev. B* **96** 195406
[62] Lucignano P, Alfè D, Cataudella V, Ninno D and Cantele G 2019 *Phys. Rev. B* **99** 195419
[63] Bernevig B A, Song Z D, Regnault N and Lian B 2021 *Phys. Rev. B* **103** 205413
[64] Mele E J 2011 *Phys. Rev. B* **84** 235439
[65] Song Z, Wang Z, Shi W, Li G, Fang C and Bernevig B A 2019 *Phys. Rev. Lett.* **123** 036401
[66] Tarnopolsky G, Kruchkov A J and Vishwanath A 2019 *Phys. Rev. Lett.* **122** 106405
[67] Pal H K, Spitz S and Kindermann M 2019 *Phys. Rev. Lett.* **123** 186402
[68] Liu J, Liu J and Dai X 2019 *Phys. Rev. B* **99** 155415
[69] Lian B, Xie F and Bernevig B A 2020 *Phys. Rev. B* **102** 041402
[70] Zhang Y H, Mao D and Senthil T 2019 *Phys. Rev. Res.* **1** 033126
[71] Kang J, Bernevig B A and Vafek O 2021 *Phys. Rev. Lett.* **127** 266402

[72] Zhang X, Pan G, Zhang Y, Kang J and Meng Z Y 2021 *Chin. Phys. Lett.* **38** 077305
[73] Lian B, Song Z D, Regnault N, Efetov D K, Yazdani A and Bernevig B A 2021 *Phys. Rev. B* **103** 205414
[74] Sboychakov A O, Rozhkov A V, Rakhmanov A L and Nori F 2019 *Phys. Rev. B* **100** 045111
[75] Isobe H, Yuan N F and Fu L 2018 *Phys. Rev. X* **8** 041041
[76] Xu X Y, Law K T and Lee P A 2018 *Phys. Rev. B* **98** 121406
[77] Huang T, Zhang L and Ma T 2019 *Science Bulletin* **64** 310
[78] Liu C C, Zhang L D, Chen W Q and Yang F 2018 *Phys. Rev. Lett.* **121** 217001
[79] Rademaker L and Mellado P 2018 *Phys. Rev. B* **98** 235158
[80] Venderbos J W F and Fernandes R M 2018 *Phys. Rev. B* **98** 245103
[81] Kang J and Vafek O 2019 *Phys. Rev. Lett.* **122** 246401
[82] Xie M and MacDonald A 2020 *Phys. Rev. Lett.* **124** 097601
[83] Xu C and Balents L 2018 *Phys. Rev. Lett.* **121** 087001
[84] Wu F, MacDonald A and Martin I 2018 *Phys. Rev. Lett.* **121** 257001
[85] Lian B, Wang Z and Bernevig B A 2019 *Phys. Rev. Lett.* **122** 257002
[86] Kozii V, Isobe H, Venderbos J W F and Fu L 2019 *Phys. Rev. B* **99** 144507
[87] Wu F 2019 *Phys. Rev. B* **99** 195114
[88] Roy B and Juričić V 2019 *Phys. Rev. B* **99** 121407
[89] Liu J and Dai X 2021 *Nat. Rev. Phys.* **3** 367
[90] Wu S, Zhang Z, Watanabe K, Taniguchi T and Andrei E Y 2021 *Nat. Mater.* **20** 488
[91] Ahn J, Park S and Yang B J 2019 *Phys. Rev. X* **9** 021013
[92] Nuckolls K P, Oh M, Wong D, Lian B, Watanabe K, Taniguchi T, Bernevig B A and Yazdani A 2020 *Nature* **588** 610
[93] Uri A, Grover S, Cao Y, Crosse J A, Bagani K, Rodan-Legrain D, Myasoedov Y, Watanabe K, Taniguchi T, Moon P, Koshino M, Jarillo-Herrero P and Zeldov E 2020 *Nature* **581** 47
[94] Schaibley J R, Yu H, Clark G, Rivera P, Ross J S, Seyler K L, Yao W and Xu X 2016 *Nat. Rev. Mater.* **1** 16055
[95] Gunawan O, Shkolnikov Y P, Vakili K, Gokmen T, Poortere E P D and Shayegan M 2006 *Phys. Rev. Lett.* **97** 186404
[96] Rycerz A, Tworzydło J and Beenakker C W J 2007 *Nat. Phys.* **3** 172
[97] Xiao D, Yao W and Niu Q 2007 *Phys. Rev. Lett.* **99** 236809
[98] Yao W, Xiao D and Niu Q 2008 *Phys. Rev. B* **77** 235406
[99] Zhang F, Jung J, Fiete G A, Niu Q and MacDonald A H 2011 *Phys. Rev. Lett.* **106** 156801
[100] Min H and MacDonald A H 2008 *Progress of Theoretical Physics Supplement* **176** 227
[101] Nagaosa N, Sinova J, Onoda S, MacDonald A H and Ong N P 2010 *Rev. Mod. Phys.* **82** 1539
[102] Xiao D, Chang M C and Niu Q 2010 *Rev. Mod. Phys.* **82** 1959
[103] Uchoa B, Kotov V N, Peres N and Neto A C 2008 *Phys. Rev. Lett.* **101** 026805
[104] Zhu Z G and Berakdar J 2013 *New J. Phys.* **15** 073028
[105] Li X, Wu F and MacDonald A H 2019 arXiv preprint arXiv:1907.12338
[106] Tritsaris G A, Carr S, Zhu Z, Xie Y, Torrisi S B, Tang J, Mattheakis M, Larson D T and Kaxiras E 2020 *2D Mater.* **7** 035028